

# Autonomous Electrical Current Monitoring System for Aircraft

M. Blagojevic, A. Dieudonne, L. Kamecki, M. E. Kiziroglou, *Senior Member, IEEE*,  
K. Krastev, D. Marty, D. Piguet, S. Spasic, S. W. Wright and E. M. Yeatman, *Fellow, IEEE*

**Abstract**— Aircraft monitoring systems offer enhanced safety, reliability, reduced maintenance cost and improved overall flight efficiency. Advancements in wireless sensor networks (WSN) are enabling unprecedented data acquisition functionalities, but their applicability is restricted by power limitations, as batteries require replacement or recharging and wired power adds weight and detracts from the benefits of wireless technology. In this paper, an energy autonomous WSN is presented for monitoring the structural current in aircraft structures. A hybrid inductive/hall sensing concept is introduced demonstrating 0.5 A resolution, < 2% accuracy and frequency independence, for a 5 A – 100 A RMS, DC-800 Hz current and frequency range, with 35 mW active power consumption. An inductive energy harvesting power supply with magnetic flux funnelling, reactance compensation and supercapacitor storage is demonstrated to provide 0.16 mW of continuous power from the 65  $\mu\text{T}$  RMS field of a 20 A RMS, 360 Hz structural current. A low-power sensor node platform with a custom multi-mode duty cycling network protocol is developed, offering cold starting network association and data acquisition/transmission functionality at 50  $\mu\text{W}$  and 70  $\mu\text{W}$  average power respectively. WSN level operation for 1 minute for every 8 minutes of energy harvesting is demonstrated. The proposed system offers a unique energy autonomous WSN platform for aircraft monitoring.

**Index Terms**—Aircraft, Electrical, Energy Harvesting, Monitoring, Wireless Sensor Network.

## I. INTRODUCTION

THE advancement of aircraft in terms of safety, efficiency, reliability, cost-effective maintenance and passenger comfort is expected to rely largely on sensing technology. This includes unmanned aerial vehicle (UAV) as well as aircraft electrification technologies [1]. New commercial aircraft models include thousands of sensors [2], while the total electrical wire length and number of connectors is as high as 500 km and 40,000 respectively [3]. Quantities including

acceleration, vibration, orientation, strain, temperature, humidity, force, pressure, displacement, speed, liquid flow and level, current, light, radiation, gravity and field, air quality, sound, as well as digital data (e.g. image, video, computer logging and communications) are monitored and recorded. They are used for services such as navigation and piloting support, control, engine and fuel monitoring, aircraft health status reporting, predictive maintenance, event diagnostics and recording, crew and passenger safety and comfort, flight profile assessment and pilot performance analysis. Beyond individual aircraft services, they can provide environmental, climate, mapping, identification of terrestrial and aerial events and conditions, and fleet coordination.

The critical importance of aviation technology in safety, security and economic terms has driven a rapid advancement of these sensing technologies and in parallel, it has led to the establishment of specific, robust solutions of high reliability and well-defined, strict standards. The emergence of internet of things (IoT) technologies, including new low power microcontroller platforms, local area network (LAN) and wide area network (WAN) wireless communication technologies, software architectures, and big, live and remote data analysis, is offering a new range of opportunities to aviation. At sensor system level recent research focuses on the development of structural health monitoring (SHM) systems. Indicatively, in [4, 5] a wireless SHM system for monitoring and impact detection on composite aircraft was implemented and tested. Wired piezoelectric arrays for smart aircraft skin were proposed in [6]. An energy autonomous strain wireless sensor network (WSN) system was developed in [7] for a specific flight testing program. Other methods for strain monitoring such as by fibre Bragg grating systems have also been proposed [8]. Furthermore, a diverse range of other sensors such as landing gear wheel force sensors [9], fiber Bragg grating temperature sensors [10], low power air pressure wireless sensors [11], active flow control WSNs [12], multi-hop aircraft vibration WSNs [13], and ultrasonic flow sensors for hydraulic systems

Manuscript received Month xx, 2xxx; revised Month xx, xxxx; accepted Month x, xxxx. This work has received funding from the Clean Sky 2 Joint Undertaking under the European Union's Horizon 2020 research and innovation programme under grant agreements No 785495 and No 886605. This document reflects only the author's view and the Commission is not responsible for any use that may be made of the information it contains. All authors contributed equally to this work and therefore, they are listed alphabetically. For the purpose of open access, the author has applied a 'Creative Commons Attribution (CC BY) licence to any Author Accepted Manuscript version arising.

M. Blagojevic and S. Spasic are with Senis AG, 6340, Baar, Switzerland.

A. Dieudonne and K. Krastev are with Safran Electrical & Power, 31700, Blagnac, France.

M. E. Kiziroglou, S. W. Wright and E. M. Yeatman are with Imperial College London, SW7 2AZ, U.K. (e-mail: m.kiziroglou@ic.ac.uk).

L. Kamecki and D. Marty are with Serma Ingenierie, 31700, Cornebarrieu, France.

D. Piguet is with CSEM, Neuchatel, 2002, Switzerland.

[14] have been developed and tested.

At sensor data analysis level, sensor fusion including Kalman filter based prediction [15] and noise tolerance [16] algorithms have been proposed for aircraft attitude control techniques. Other indicative techniques developed for aircraft include neural network and long short-term memory (LSTM) models for hard landing prediction [17] and machine learning for damage identification [18].

At network level, a variety of networking architectures and techniques have been studied for aircraft applications, including cooperative schemes [19], structural acoustic wave communication [20], sensor deployment optimization [21], dynamic reconfigurability [22] and game theory based medium access control (MAC) protocol design [23]. An overview of ad-hoc aeronautical networking technology can be found in [24] and an assessment of wireless networking benefits for avionics has been presented in [25].

As it is the case with most established heavy industries, the adoption of these fast emerging technologies has been slow, due to regulation and compatibility challenges, the requirement for new investment, and prioritization to capitalizing on technologies adopted just a couple of decades ago, which is a short timeframe compared to aircraft lifetime. Beyond this expected latency, the key missing element in applying IoT sensing is the requirement for powering individual sensors, which reduces the benefit of wireless operation. Wire-powering or adding battery replacement maintenance requirements are impractical. Wiring and maintenance simplification is highly desirable and a prime objective of adopting new sensing technologies in the first place. Therefore, energy harvesting and wireless power transfer technologies are especially valuable in aircraft applications.

Aircraft sensor systems powered by heat [26-29], vibration [30], flow [31], static charge [32] and by inductive coupling to the electrical power network [33-36] have been considered. Inductive power transfer methods [37, 38] have also been implemented. Typically, such systems include low power sensing, microcontroller and RF communication electronics. In [7], a low power WSN protocol combined with multiple Sensor Node (SN) functionality modes and programmable duty cycling for all subsystems was introduced. Overviews of energy harvesting technologies for aircraft and specifically for aircraft SHM applications can be found in [39] and [40] respectively. A general key limitation of energy harvesting technologies is the environmental uncertainty and variety, which leads to the requirement for bespoke solutions, customized to the specific application environment. The aircraft offers a certain and relatively predictable environment for technology development and has thereby enabled some of the first functional energy autonomous WSN demonstrations.

In this paper, an energy autonomous aircraft current monitoring system is introduced, designed for measuring the current flow through the aircraft structural beams, which are used as the return current path of its main electrical power installation. It comprises a differential hall sensor system, an inductive power supply developed for coupling to structural currents, a low power microcontroller and RF communication

unit, and a low power protocol developed for enabling sub – mW average power operation while addressing certain aircraft and sensing scenario specifications. The overall system design is confined to industrial aircraft specifications and a certain sensing use case. Its performance is evaluated on a full-size industrial aircraft beam setup, including qualification evaluation for flight testing.

The rest of this paper is organised as follows: The aircraft sensing use case is described in Section II. In Section III, the sensor node architecture including control and communication, sensor and front-end electronics, power supply and packaging are presented, followed by a description of the network architecture in Section IV. An evaluation summary of the system as a whole is given in Section V. A conclusion and an outlook for further use and development are presented in Section VI.

## II. SENSING REQUIREMENTS

The structural current monitoring system design is based on an aircraft sensing use case. The return current of typical aircraft electrical networks passes through the aluminum alloy structural beams of the airframe. As the role of electricity in aviation is extended to new functionalities, the effect of increased current flow to the electrical infrastructure needs to be evaluated. More specifically, the distribution of the return current path to the structural beam network is of key interest, as beam-to-beam junctions may be affected, resulting in heating, contact degradation (potentially including electromigration effects) and high contact resistance which can increase the risk of hazard. In addition, the prospect of composite aircraft requires an evaluation of the electrical return path in order to consider alternative solutions. The objective of the sensing use case is to provide a dynamic mapping of current distribution through the aircraft airframe during flight.

A priority for aircraft sensor networks is wireless functionality and energy autonomy, due to the increased significance of weight reduction and infrastructure simplicity in aircraft installations. Therefore, a wireless, energy autonomous and non-invasive monitoring system for aircraft structural currents is targeted.

The current measurement range and resolution is set to 5 A – 100 A and 0.5 A respectively, for direct current (DC) as well as for alternating current (AC), in root-mean-square (RMS) values, with a frequency range between 360 Hz and 800 Hz. This frequency range correspond to specifications of variable frequency electrical generators used in aircraft since the Boeing B787 Dreamliner and Airbus A380 programs [36, 41]. These generators are directly connected on the motor's shaft and hence their frequency depends on the engine speed & the number of poles employed. The expected minimum average AC current availability is set to 20 A RMS. This value was defined by an internal study in which the aircraft structural current distribution of over 700 electrical loads, supplied using 28V, 115 V or 230 V was analyzed.

A population of up to 300 SNs and a 30 m wireless communication range is defined. Power autonomy adequate for system cold starting and data acquisition once every 8 minutes is required. A total mass for each sensor node in the 50 g range

is desirable for practical installation. Synchronization among SN in the 1 ms range is also desirable. These use case specifications were defined by Safran Electrical and Power S.A., based on internal studies and towards an experimental onboard health monitoring system of the current return network. In such a system, the statistical distribution of current and its local variations can be used to monitor the status of contact resistances on the aircraft structure.

### III. SENSOR NODE ARCHITECTURE

#### A. Overview

In order to provide the sensing service described in Section II, a custom sensor node architecture has been developed. It is based on the Nordic Semiconductor NRF52840 System on Chip, which combines an ARM Cortex M4 microcontroller with a 2.4 GHz low power communication transceiver. The structural current is measured by a differential pair of combined hall-effect and inductive sensors, driven and read by an advanced low-power front end circuit. Both systems are powered by an inductive energy harvesting power supply that collects energy from the AC magnetic flux around the current carrying structure. The power supply includes a power management system based on the Texas Instruments BQ25570 microchip, dual voltage regulation and super-capacitor energy buffering. All systems are integrated into a package suitable for installation on the aircraft structural beams described in Section II. Digital and analogue electrical interfacing is implemented through standard connectors and an auxiliary printed circuit board (PCB). A block diagram of the sensor node architecture is illustrated in Fig. 1.

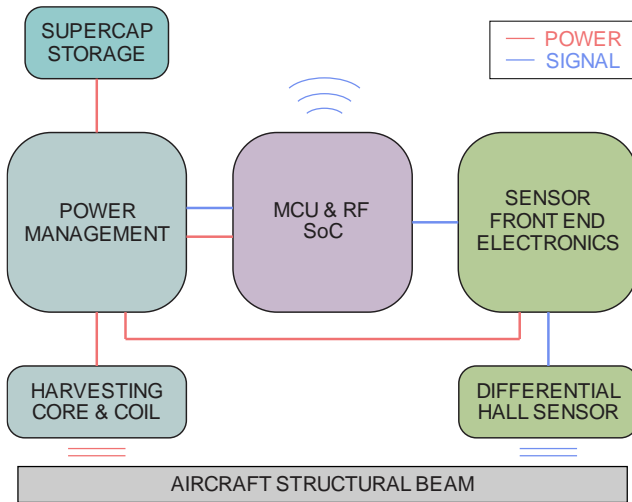


Fig. 1: Block diagram of the Sensor Node.

The overall design, the prototyping of submodules and components, and the software development are focused on achieving energy autonomy, within the functional specifications required for the use case of Section II. The power consumption of each submodule, measured by monitoring the total current feed to the corresponding PCB for different operation modes is summarized in Table I. Each module can be controlled to operate in one of several duty cycle regimes among shut down, sleep and one or more active modes. The sensor node may operate in three different functionality modes:

network association, data acquisition/transmission and sleep. Each operating mode uses different duty cycling scenarios, resulting in different average power requirements. The overall average power consumption must be covered by the average harvested incoming power, and higher power modes can be accommodated by the supercapacitor energy buffer for short operating durations. Therefore, power autonomy performance depends not only on energy harvesting provision and electronic component consumption but also on sensor node operation scheduling and on the network protocol. An evaluation of the energy and power budget of the overall system is presented in Section V, after a description of the sensor node modules in the rest of this section and a description of the low power protocol introduced in Section IV.

TABLE I  
MEASURED POWER CONSUMPTION OF THE SENSOR NODE

Module	Mode	Current mA	Power mW
NRF52840 SoC	Active, Acquisition	3.6	6.48
	Active, TDMA TX	25.2	45.4
	Active, TDMA RX	14.5	26.1
	Sleep	0.002	0.0036
Senis AG Structural Current Sensor	Acquisition	7	35 (5V)
	Sleep	< 0.001	< 0.005
Total Sensor Node	Max	32.2	80.4
	Sleep	< 0.003	< 0.0086

#### B. Communication Module

The communication module is implemented in the 25 mm by 25 mm PCB shown in Fig. 2. This PCB was designed and fabricated specifically for the system presented in this paper and can be used both in sensor node (SN) and wireless data concentrator (WDC) modules. The central element is a Nordic Semiconductor nRF52840 communications and microcontroller unit (MCU) system-on-chip (SoC), chosen for its higher flash and random access memory (RAM) compared to other Nordic MCU models. The nF52840 provides 2.4 GHz low power communication, supporting the Bluetooth Low Energy (BLE) standard, IEEE802.15.4, as well as proprietary communication modes. The MCU is a powerful, yet low power consumption, 64 MHz Arm Cortex M4 with 8 Analogue to Digital Converter (ADC) channels and a rich set of the digital interfaces including serial peripheral interface (SPI), inter-integrated circuit (I2C) and universal asynchronous receiver transmitter (UART). Its 1 MB program memory and 256 KB RAM are large enough to support complex communications protocols as well as most sensing and actuation applications.

The UART interface is used for wire data transfer from the WDC modules. Nine General Purpose Input/Output (GPIO) ports are used for digital communication with the sensor module described in Section III.C. Three of the ADC channels are employed for analogue voltage readings from the sensor module and one is dedicated to monitoring the supercapacitor voltage status. An SPI interface is intended for long-range (LoRa) network communication. The I2C interface is included for future system extensions and can accommodate temperature and humidity sensors as well as authentication hardware. The LoRa, I2C and BLE interfaces are not utilized in the work presented in this paper.

An external real time clock provides the system alarm clock and metronome. The ability to program a wake-up interrupt enables the nRF52840 to be completely shut down and awoken the next time it is needed. The low deviation of the real time clock, compared to a quartz clock, allows ultra-optimized implementation of the time division multiple access protocols (TDMA, see section IV), with minimal guard times to compensate deviations, even with large intervals between communication events.

The board also includes a secure element that supports a wide range of security functionalities including confidentiality, data integrity, and authentication with hardware-based cryptographic key storage and cryptographic countermeasures, which eliminate potential backdoors linked to software weaknesses. The communication PCB architecture is depicted in Fig 3. The overall PCB mass is 2.4 g.



Fig. 2: The communication PCB (25 × 25 mm)

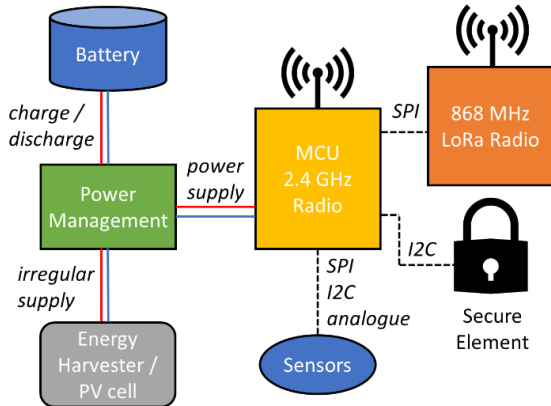


Fig. 3: Block diagram of the communication PCB.

C. Structural Current Sensor

The current flow through the structural beam is measured indirectly, through the magnetic field around the beam. Although the current frequency is relatively low (1 < kHz), the skin effect is significant, due to the large size of the beam cross-section [36]. Indicatively, at 300 Hz the skin effect depth is below 5 mm for an aluminum conductor, which is smaller than the beam cross section dimensions. The AC current is thereby pushed to the beam edges. The current distribution is non-uniform and frequency-dependent. Indicative simulations demonstrating this effect are shown in Fig. 4. Therefore, careful simulation and experiments are required in order to define an

optimal position of the current sensor on the structure. The implemented current sensor combines a Hall sensor and a pick-up coil oriented as shown in Fig. 5. The Hall based sensor was selected due to its DC and AC magnetic field measurement accuracy and its small dimensions and weight.

In order to achieve the required magnetic resolution, i.e., the required signal-to-noise ratio, for the sensor biasing and for the detection of the Hall voltage a “spinning current” technique was applied [42]. A low-pass filter LPF1 as shown in the block diagram of Fig. 6 is applied to reduce the noise, but it limits the frequency bandwidth. As shown in Fig. 4, the magnetic field measured with the Hall sensor depends on the frequency of the AC current through the beam. Due to a complex geometry of aircraft structural beams, it is very difficult to determine a Hall sensor mounting position that would ensure a frequency-independent measurement of the magnetic field. Therefore, the output signal of a pick-up coil is added to the Hall sensor output signal. The Hall sensor is positioned in the middle of the structural beam, while the pick-up coil is laterally displaced as shown in Fig. 5. An increase in current frequency will cause a decrease of the Hall voltage due to the lateral skin effect, while the pick-up coil output voltage will increase. The pick-up coil detects the AC only and its induced voltage is proportional to  $dB/dt$ . Therefore, an integration step is required. This is implemented by the low-pass filter LPF2 shown in Fig. 6. By an appropriate selection of LPF1 and LPF2, a flat frequency response of the whole current sensor system was obtained in the full frequency range. A very high immunity on stray fields was obtained by using a system of a couple of Hall sensor and pick-up coil positioned asymmetrically in an antiparallel configuration, which cancels the influence of the external magnetic field. The current consumption of the whole system is additionally reduced by applying a duty-cycle operation mode.

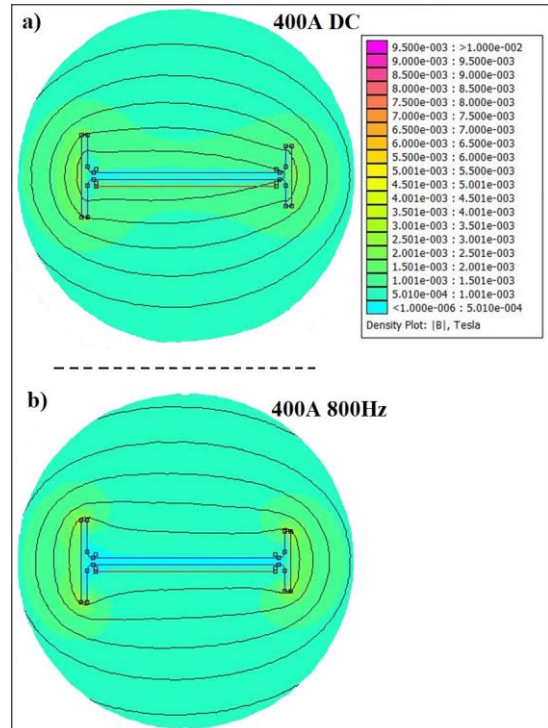


Fig. 4: Simulated redistribution of the magnetic field due to the lateral skin effect in an H-shaped beam for a) 400 A DC current; b) 400 A AC current.

The communication between the MCU and the Sensor PCB, illustrated in the block diagram of Fig. 6, includes nine GPIO ports for digital control of activation, gain configuration and sequencing the spinning current sensing technique. It also includes three analogue channels for reading the AC and DC current measurements and the sensor voltage reference, connected to three of the MCU ADC channels. A photograph of the sensor system on a full scale aircraft structural beam is shown in Fig. 7.

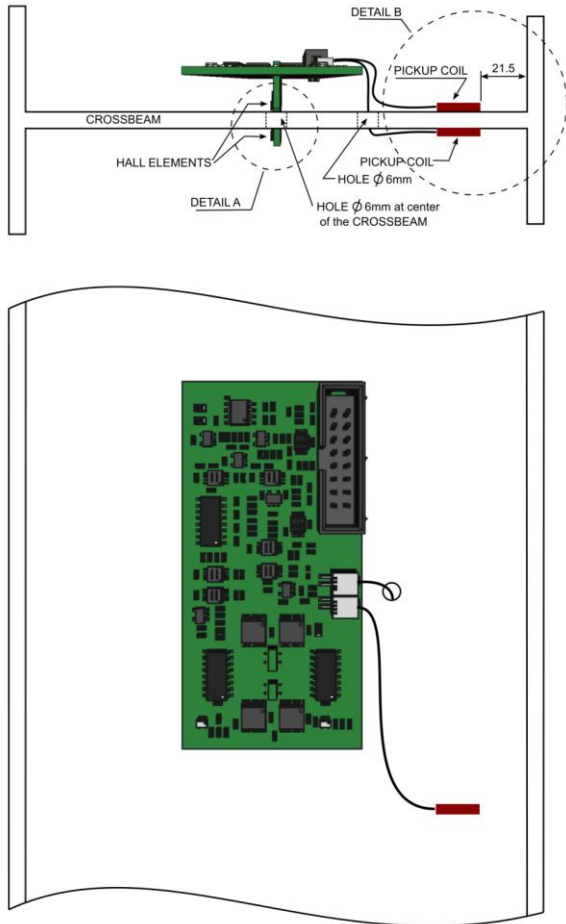


Fig. 5: Current sensor design comprising a couple of Hall sensor and pick-up coil positioned asymmetrically in an antiparallel configuration.

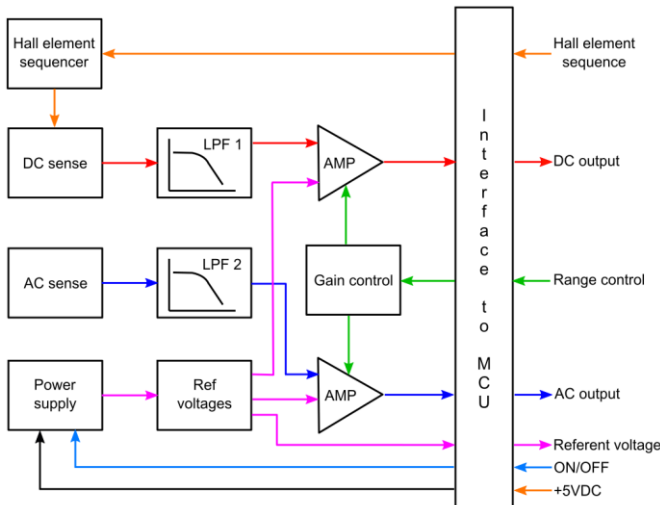


Fig. 6: Functional block diagram of the structural current sensor.

Indicative performance results of this sensor system are presented in Fig. 8. A linear relationship between the structural current amplitude and voltage output is observed both for DC and AC measurements, with a distortion for currents over 15 A RMS at 500 Hz and 800 Hz. While the hall/inductive sensor combination demonstrate remarkable frequency invariance between 500 Hz and 800 Hz, the 360 Hz shows a significant deviation. This deviation could be compensated by hardware or data analysis calibration. For example, the difference between the hall and inductive voltage outputs which is largely frequency dependent could be exploited as a measure of frequency and taken into account in the analog and digital signal processing towards a calibrated structural current measurement. The output voltage to structural current correlation shown in Fig. 8 demonstrate a worst-case resolution and analysis of 1% and 2% respectively, limited by the signal-to-noise ratio of the voltage output of the hall and inductive transducers. The Hall and inductive voltage outputs are fed to the ADC channels of the MCU, allowing translation from voltage to current in the digital domain. The demonstrated performance of the developed structural current sensor is summarized in TABLE II.

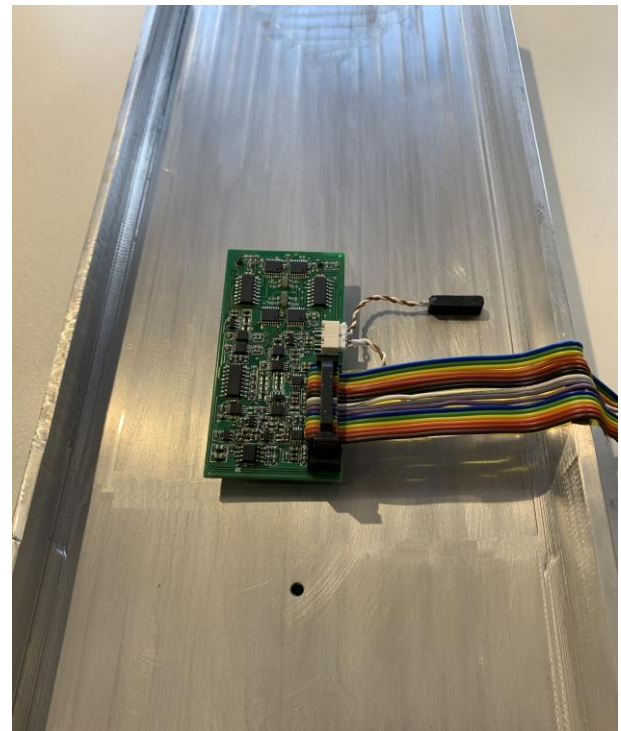


Fig. 7: Photograph of the structural current sensor.

TABLE II  
SUMMARY OF THE STRUCTURAL CURRENT SENSOR FEATURES

Feature	Value
Current / magnetic sensitivity	5 mV/A, 2.5 V/mT
Measurement range	5A – 100A
Frequency range	DC – 800 Hz
Resolution	<1% (0.5A)
Accuracy	<2% (1A) @ 50 A
Current consumption:	7 mA at 5 V DC
Total dimensions and weight	75 mm × 37 mm, 17g

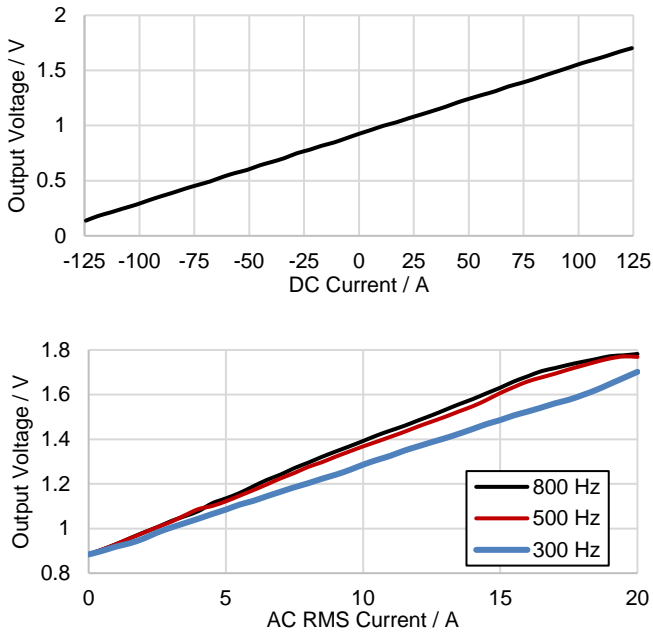


Fig. 8: Up: Voltage output vs DC current. Down: Voltage output vs AC current.

**D. Power Supply**

The power supply module comprises an inductive energy harvester suitable for collecting power from structural currents and a power management system. The energy harvesting concept is illustrated in Fig. 9. A coil with a soft magnetic core is coupled to the magnetic field around the structure, by installation at an edge location where a higher magnetic field is available due to the skin effect, as illustrated in the inset. A funnel core shape is employed to guide flux from a given area through a smaller cross-section, thereby amplifying flux density and increasing the voltage and power output. A transducer design with optimal coil/core mass ratio is used for maximum transducer power density. These two methods have been introduced in [34, 35] and can provide combined power density increase of as high as two orders of magnitude. An earlier version of this type of energy harvesting was presented in [36], using a different power management system.

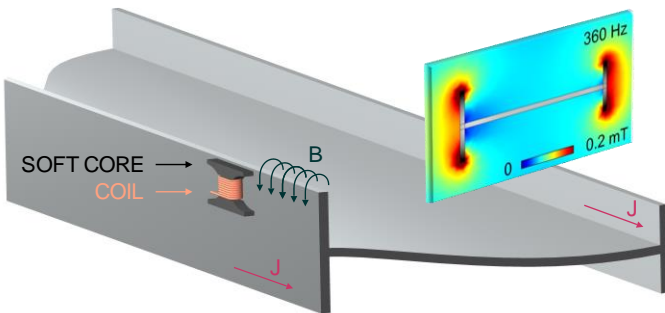


Fig. 9: The concept of inductive energy harvesting from structural current running through an aircraft beam. Inset: indicative simulated magnetic flux density distribution of a 25 A RMS, 360 Hz current illustrating the skin effect.

A photograph of the energy harvester used for the sensor node presented in this paper is shown in Fig. 10. It is based on a 10,000 turn, 60  $\mu$ m Cu wire coil of 6.7 g mass which forms a 20 mm long hollow cylinder with 5 mm and 11 mm inside and outside diameter respectively. The coil was custom-wound by

North Devon Electronics Ltd. An H-shaped core is employed comprising a 20 mm long, 5 mm diameter ferrite central rod with nominal magnetic permeability  $\mu_r = 250$  and two 70 mm  $\times$  12 mm  $\times$  0.5 mm lateral plates (flanges). The flange material is a NiFe alloy with 80% Ni and nominal  $\mu_r = 30,000$  from Holland Shielding Systems B.V. [43]. The parts were assembled in a custom 3D-printed acrylonitrile butadiene styrene (ABS) box, such that the coil is placed around the central rod of the H core. The mass of the coil, rod, each flange and box are 6.7 g, 1.8 g, 3.6 g and 7.2 g respectively, yielding a total of 22.9 g, including a sliding lid, not shown in Fig. 10.

The open circuit performance of this transducer has been characterised in a spatially distributed 0.12 mT RMS magnetic field in [44]. This corresponds to structural currents of around 36 A RMS in the use case of Section II [36]. Results demonstrate an output range of 1 - 5 V for the 300 Hz – 800 Hz aircraft current frequency range. Taking into account the (as measured) 1.6 k $\Omega$  ohmic coil resistance and assuming perfect reactance cancellation, this voltage range corresponds to a power range between 0.7 mW and 5 mW. Further details on the standalone performance of this energy harvester can be found in [44].

The power management architecture of the power supply is illustrated in Fig. 11. It is based on a voltage doubler rectifier in combination with boost and buck converters for supercapacitor energy storage and regulated voltage provision.

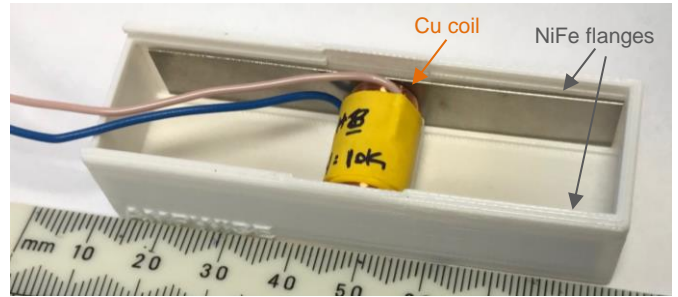


Fig. 10: The inductive energy harvesting transducer (sliding lid not shown).

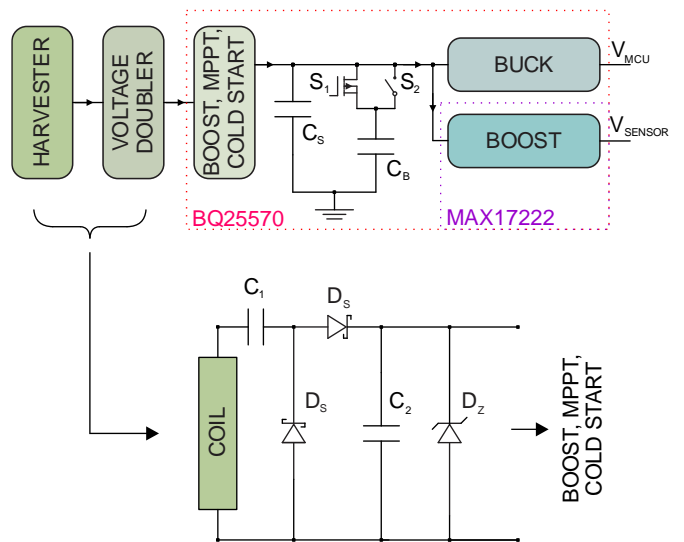


Fig. 11: Architecture of the energy harvesting power management system.

The voltage doubler circuit is implemented with Schottky diodes  $D_S$  exhibiting 0.2 V forward voltage drop at 2 mA and reverse leakage below 2  $\mu\text{A}$  at 5 V [45]. The doubler input and output capacitors are  $C_1 = 26 \text{ nF}$  and  $C_2 = 100 \mu\text{F}$  respectively, with the first also serving as reactance cancellation for the inductive transducer. This  $C_1$  value corresponds to reactance cancellation at 360 Hz for the given transducer coil. Tuning the reactance cancellation to a low frequency value is selected because, as power scales with the square of frequency, this provides a stable power level over the frequency range, as has been shown in [36]. Finally, the voltage doubler circuit includes a 5.1 V, 50 mA Zener diode  $D_Z$  for overvoltage protection.

Subsequently, the rectified output is boosted to a higher voltage level (up to 5.5 V) to allow efficient storage on a supercapacitor,  $C_S$ . For this purpose the Texas Instruments BQ25570 is employed [46], which also includes a cold starting booster, maximum power point tracking (MPPT), secondary storage capability ( $C_B$ ) and a buck converter for selectable regulated output. The MPPT system ensures that the voltage at the chip input is maintained at half the open circuit voltage of the voltage doubler (i.e. the voltage on  $C_2$ ), as charge is pumped from  $C_2$  to  $C_S$ . Thereby, the power transfer efficiency from the inductor to  $C_2$  is nearly maximized. Further increase could be possible by taking into account the effect of rectification to the configuration of the maximum power point [47]. To obtain a fast transition to the more efficient active mode boosting, the value of  $C_S$  should be selected to be small enough for a fast charge. On the other hand, this limits the energy buffer size provided by  $C_S$ , which is critical for the high-power driving capability of the power supply and the energy autonomy of the sensor node. To address this conflict, a larger secondary supercapacitor  $C_B$  is used, which can be connected to the circuit only while the voltage on  $C_S$  is high enough to ensure active boosting. This is implemented by an enhancement mode p-channel MOSFET switch ( $S_1$ ) in Fig. 11. A disadvantage of this implementation is that  $C_B$  is still being charged through the MOSFET body diode when the MOSFET is off, leading to inefficient charge transfer. Therefore, in certain conditions and depending on cold-starting speed it may be beneficial to connect the positive terminals of  $C_S$  and  $C_B$  together. This option is provided by a hardware switch ( $S_2$  in Fig. 11).

Finally, two regulated output voltages are provided through an output buck converter (included in the BQ25570 chip) and an additional Maxim MAX17222 booster [48]. The first voltage is set to  $V_{MCU} = 1.8 \text{ V}$  in order to supply the nRF52840 SoC at its lowest power consumption voltage level. The second voltage is set to  $V_{SENSOR} = 5 \text{ V}$ , supplying the sensor front end circuit as required. The two voltage supply rails are also shown in Fig. 11. To reduce the overall power consumption, the MAX17222 is activated by the MCU only during acquisition, allowing startup time for the front-end electronics as needed.

As mentioned, the required energy buffer depends on the sensor operation mode schedule which is software determined and based on the data acquisition and communication protocol scenarios. For this reason,  $C_S$  and  $C_B$  are implemented as external, selectable components. The BQ25570 circuit is implemented on the communication PCB (Fig. 2), while the rest of the circuit is implemented as a separate PCB.

The power supply has been tested both under emulated magnetic fields and on a full-scale industrial aircraft beam rig, in integration with all sensor node electronics. The harvester output power measured on an ohmic load as a function of structural current amplitude is shown in Fig. 12, with a photograph in the inset. Indicative results of the full power supply start-up from a completely discharged condition (i.e. zero voltages on all capacitors and no other power sources) are shown in Fig. 13. The aircraft structural beam was supplied with a 20 A RMS, 360 Hz for this test. A low leakage 100  $\mu\text{F}$  electrolytic capacitor and a 50 mF supercapacitor were used as  $C_S$  and  $C_B$  respectively. The  $C_B$  charging curve is plotted, for  $S_2$  in closed state, i.e. with  $C_B$  connected in parallel with  $C_S$ .

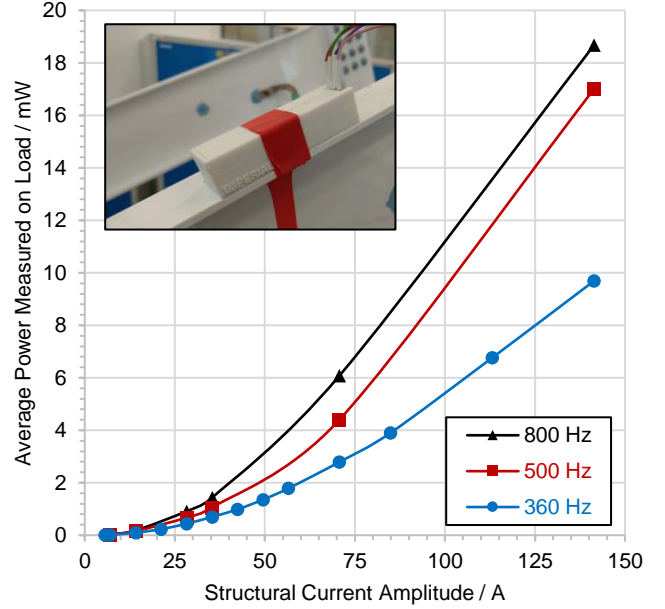


Fig. 12: Harvester output power measured on an ohmic load at half-open-circuit voltage conditions. Inset: The device installed on the industrial test rig.

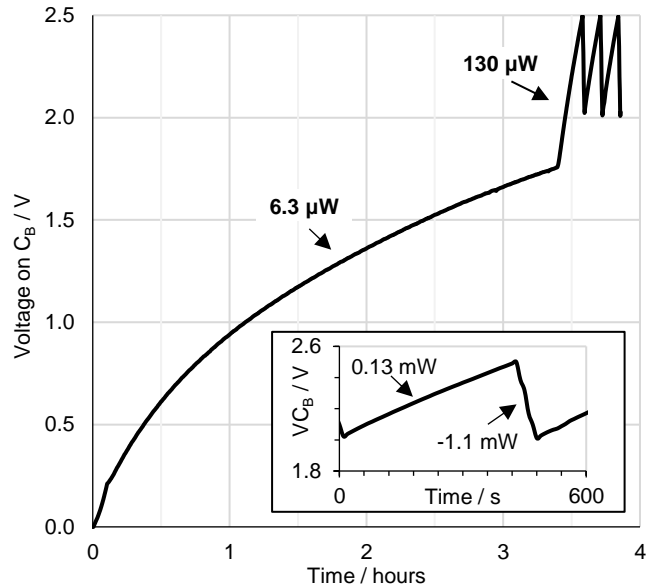


Fig. 13: Power supply cold-starting, under the field of a 20 A RMS, 360 Hz structural current. The supercapacitor voltage increase from zero to activation of sensor node operation is presented, for  $C_B$  connected to  $C_S$  directly with  $S_2$  closed (green curve). Inset: The active charge / sensor operation loop.

The system undergoes a cold-starting energy harvesting process of 3 hours and 23 minutes with an average power income of  $6.3 \mu\text{W}$ . When the voltage on  $C_S$  reaches 1.8 V, the more efficient active voltage boost converter of the BQ25570 chip is activated and a faster charging phase occurs ( $130 \mu\text{W}$  average power income), leading to a sensor node system startup when the output activation threshold is reached, which has been set at 2.5 V (during rising), after another 7 minutes. The sensor node carries out its startup and network association protocol and operates for around 1 minute at 1 mW average power (as detailed in the inset of Fig. 13, until it is cut-off by the power management falling threshold control, set at 2 V to maintain the power management system in active mode. Subsequently, another round of voltage rising occurs towards 2.5 V.

The results of Fig. 13 demonstrate a sensor node cold-start within 3 hours and 30 minutes from a 20 A RMS, 360 Hz aircraft structural current. A power input of 0.13 mW is achieved, as measured on the storage supercapacitor in active power management mode. This demonstration includes all quiescent and off-state power leakage of the complete system, as well as self-leakage of all capacitors. For practical testing, the output enable thresholds was set to 2.5 V, leading to a sensor node functionality time of around 1 minute every 8 minutes of energy harvesting. An increase of the output threshold to 5 V can provide a 10-fold increase of the energy buffer, which could offer longer sensor operation times at the expense of a moderate increase of cold-starting time. On the other hand, using a lower supercapacitor value could allow faster cold-starting in the same conditions (indicatively around 20 minutes with 5 mF), but with a reduced energy buffer. Finally, for these tests, the sensor node was programmed to startup, associate to the network and start a low duty cycle measurement cycle in accordance with the sensing scenario of Section II. In deployment, the sensor node can be programmed to measure its energy buffer state and adjust its operation cycle accordingly in order to prevent, or intentionally choose a complete power off, depending on network level sensing data demand.

### E. Integration and Packaging

This integration task of the autonomous current sensor consists of providing a compact module, easy to install on board without any modification of the aircraft beam and offering a good antenna orientation for the wireless communication. An optimal position for the AC and DC current sensors is important for sensitivity. In addition, the harvesting transducer should be located at the beam edge, in order to take advantage of the increased field density in this location, due to the skin effect. Interference between the sensor and the power transducers must be minimal. The enclosure needs to be robust and to electrically isolate the sensor node from the aircraft beam.

The overall integration package is illustrated in Fig. 14. The harvester is placed by a beam flange edge, as shown at the bottom of the cross section drawing in Fig. 14, left. The sensor electronics PCB and the communications PCB lie in the center of the beam and are illustrated in green and red respectively. According to the sensor element specifications described in Section III.C, the DC sensor needs to be placed in the middle of the structural beam whereas for the AC sensor an edge location

is preferable, again due to the more intense AC magnetic field, at adequate distance from the harvester to minimize interference. To ensure efficient wireless links, the enclosure shall not disturb the antenna with conductive parts. In this implementation a PCB antenna has been selected for installation simplicity, although the option of an external antenna is also provided.

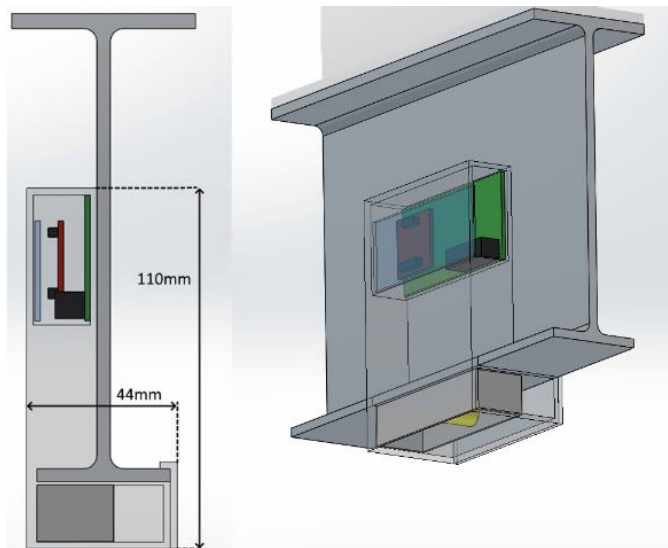


Fig. 14: Cross section (left) and three dimensional (right) view of the aircraft beam showing the sensor packaging geometry and arrangement.

A photograph of the implemented enclosure is presented in Fig. 15. The enclosure is 3D printed by an Ultimaker 3D-printer in two main parts. The box on the left is to be installed on one side of the aircraft structural beam. It holds the energy harvesting power supply and all the PCBs. The part on the right of Fig. 15 is to be installed on the other side of the beam, in attachment with the left part around one of the beam flanges. This part holds one of the differential AC current sensors. The assembly of the two parts around one side of the beam provides: a) A locking mechanism for a fixed installation of the whole package to the avionic structural beam. b) A sub-mm accurate installation alignment using the beam flange as guide, which in turn allows alignment of the harvester and sensor locations.

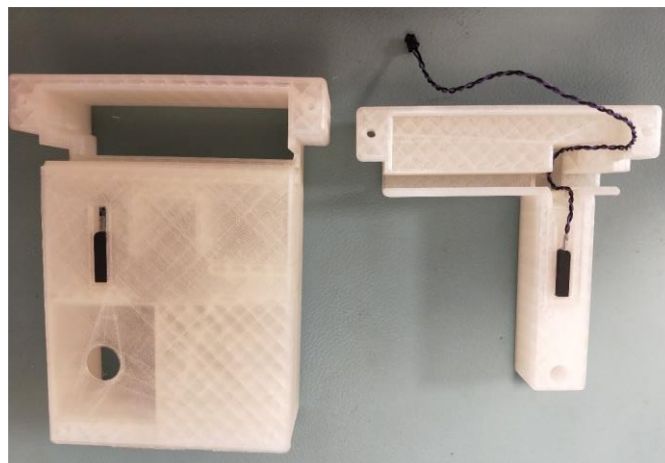


Fig. 15: Photograph of the sensor node enclosure package comprising two parts.

c) Differential field sensing on either side of the beam for an accurate structural current calibration and measurement. An open-lid photograph of the complete sensor node installed on a full-scale aircraft structural beam for testing is presented in Fig. 16. In the photograph, the energy harvesting power supply (white box in the slot on the right), control and communications PCB (red PCB), connections and power management board (top green PCB) and sensing front end electronics board (bottom green PCB) are illustrated.

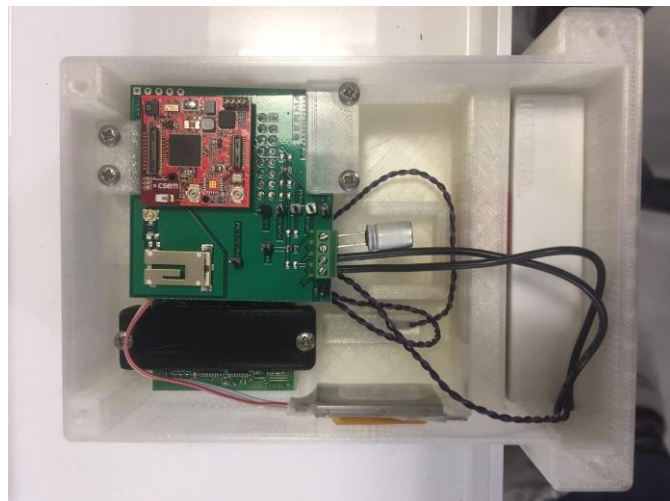


Fig. 16: Photograph of the sensor node package under test, installed on a full-scale industrial aircraft beam.

The red communications PCB includes all digital and RF electronics. It also includes the BQ25570 circuitry of the power management system as described in Section III.D. The interfacing / power management board was designed to provide connectivity among all subsystems. It includes a voltage level shifter, employed to adapt the bus communication voltage levels between the wireless communication unit and the current sensors section. It also includes the voltage doubler and MAX17222 circuitry of the power management system described in Section III.D. Finally, it includes inter-PCB connectors, connectors for up to two supercapacitor storage elements and additional access points for circuit configuration and testability during system performance evaluation. A photograph of the three interconnected PCB boards is shown in Fig. 17.

#### IV. NETWORK ARCHITECTURE

##### A. Overview

The network architecture is a multi-star topology: the aircraft is equipped with Wireless Data Concentrators (WDC) which each have a wired connection to the avionics. Each WDC is associated to a group of Sensor Nodes (SN). The WDC is the TDMA master: it sends regular beacons which assign transmission slots to the sensor nodes. The WDC also propagates the global system time to timestamp the sensor data, which are forwarded to the avionics over the wired network.

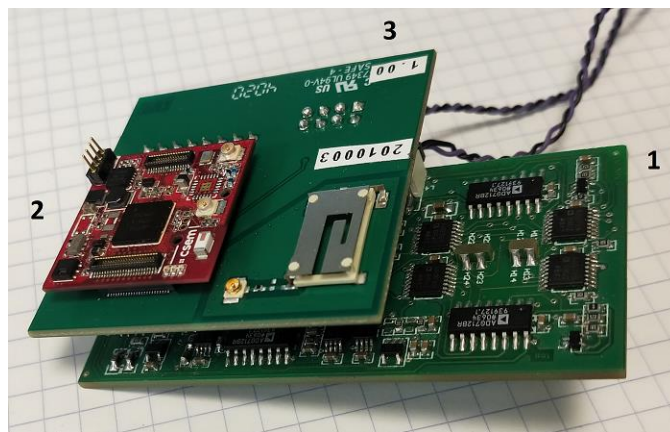


Fig. 17: Photograph of the sensor node electronics including (1) the Senis AG front end electronics PCB, (2) the communication PCB and (3) the SERMA/Imperial power management and interfacing board.

##### B. Protocol

Given the star topology, the communication protocol challenge is with the MAC (Medium Access Control) layer. According to Langendoen and Meier [49], MACs for WSNs may be categorized into random access, slotted, frame-based and hybrid protocols. Slotted MAC (S-MAC) operation is distributed along a sequence of activity and sleep cycles. During the active part of each cycle, nodes exchange information using some form of contention access. S-MAC [50] has a fixed duration thus limiting the maximum traffic to the duty cycle between the active part and the cycle time, whereas timeout-MAC (T-MAC) [51] adapts the size to the traffic. The IEEE 802.15.4 standard in its beacon-oriented version is another example. They all have the drawback of grouping all the exchanges at the beginning of the cycle thus increasing the probability of collision and limiting the traffic. A survey of MAC protocols for IoT and WSN applications can be found in [52].

Frame-based protocols are elsewhere called TDMA protocols. In general, schedules are difficult to establish, especially in presence of moving nodes or fluctuating link quality. In particular, handling retries due to transmission errors leads either to complex schemes or large inefficiency. TDMA-based solutions are very efficient in high and constant loads. Low but still constant loads may also be handled efficiently by compensating clock drift as in [53]. Solutions have been designed to manage efficiently variable loads, at the expense of higher complexity [54]. Minimizing energy consumption has been investigated in a number of papers (see for instance [55]) using scheduling techniques. The basic idea is to save energy by scheduling nodes to work in their own time slot and change to sleep state when nodes are out of their own time slot.

Hybrid protocols such as Crankshaft [56] combine TDMA with the carrier sense multiple access (CSMA) protocol to reduce collision probability and improve efficiency in presence of low or variable traffic. In random access, nodes contend for the medium with the risk of collisions. WiseMAC [57] is an ultra-low power contention MAC created at CSEM that uses preamble sampling and pairwise exchange of schedules to reach close to ideal performances in medium to low traffic conditions. Despite some limitations, pure TDMA protocols are preferred in avionics for ease of certification.

Therefore, to comply with the deterministic requirement of aviation, the protocol adopted in this work is a pure TDMA protocol, the base of which was laid in a previous work [7]. The protocol is multimode, in the sense that although the WDC sends beacons regularly with a 100 ms interval, sensor nodes adapt their duty cycle to the current mode of operation. The first mode is association, in which SN scan all system channels every 10 minutes until they find a WDC that advertises their address. Once the association is done, the SN enter the sleep mode during which they wake-up to receive the WDC beacon every 2 seconds. This keeps them synchronized and reachable within a reasonably short time, while maintaining a low duty cycle to minimize power consumption (1.6 ms of beacon reception, almost 2 s of sleep time). The third mode is the data transfer mode: sensor nodes receive all WDC beacons (thus every 100 ms) and transmit sensor data in the slots assigned by the WDC. They can sleep outside these activities. An addition compared to [7] is the automatic retransmission slot allocation by the WDC, implemented to compensate for transmission failures without increasing latency too much.

The use case of the system presented here, as outlined in Section II stipulates the acquisition of an AC-DC current sample every 5 minutes. Although in previous versions of the protocol the communication mode (sleep to data transfer) was set by the avionics, for this work, intelligence was added to the WDCs so that they operate autonomously: upon trigger from the avionics, the WDC manages the sensor acquisition autonomously: 5 minutes in sleep mode (SNs receive a beacon every 2s), then the WDC triggers the data transfer mode and requests sensor data. Sensor nodes activate the current sensor and transmit the data in the next available TDMA slot allocated by the WDC. The WDC switches back to sleep mode as soon as it has received the data from all its associated SN, including retransmissions of lost packets. This minimizes the time spent in data transfer mode, resulting in a drastic reduction of power consumption.

The communication system power consumption was measured using a Keysight CX3324A current waveform analyzer. Average current and duration of each possible activity mode were measured, then the duty cycles were accounted for, to compute the overall average power consumption.

Table III shows the current and duration measured for each activity. The SN has two sleep modes: deep sleep and sleep with RAM data retention. In deep sleep, the processor is turned off and its next wake-up is triggered by the real time clock (RTC). RAM data is lost. Recovery from this state requires a significant wake-up process energy. Therefore, deep sleep is beneficial for operation modes involving long sleep duration, such as the association mode. When the SN wakes-up to associate, it may scan up to 20 channels for 100 ms each (interval between two beacons). When associated and the 5 minutes period current sensing application is active, the sensor node either sleeps with RAM retention, receives a beacon or receives a beacon, acquires measurements on its ADC and sends one measurement packet. In sleep mode, there is a 2 second period between beacons receptions. In data transfer mode, this period is 100 ms. Hence, in association mode, the average current consumption of the SN communication system is 39  $\mu\text{A}$  (70 mW). This value can be reduced to a minimum of 3  $\mu\text{A}$  if a single channel is reserved for association.

TABLE III  
CURRENT CONSUMPTION OF THE SN COMMUNICATION SYSTEM AT 1.8 V

Activity	Duration	Current
Deep sleep (unassociated, wake from RTC)	10 minutes	2 $\mu\text{A}$
Scanning 20 channels	2 seconds	10.9 mA
Sleep (RAM retention)	2 s / 100 ms	20.6 $\mu\text{A}$
1 beacon reception	1.6 ms	5.06 mA
Beacon, measurement, transmission	5 ms	6.84 mA

In acquisition mode, taking into account the beacon reception and data acquisition/transmission rates, and given the average of four beacon receptions during measurements (i.e. until the WDC goes back to sleep mode), the average current consumption of the sensor node communication system is 25  $\mu\text{A}$  (45 mW). If the acquisition period is reduced to one minute, the average current consumption would be 25.6  $\mu\text{A}$ , hence not much higher. This demonstrates a sleep-mode dominated power consumption which provides room for more frequent data acquisition. In challenging RF communication conditions, it is possible that a SN misses beacons resulting in transmission error and repetition. However, the impact of repetition to power consumption is low, due to the small duty cycle. Indicatively, an additional 0.1  $\mu\text{A}$  of average current can be accounted for each repetition, including the reception of the additional required beacons. This performance is achieved due to the state-of-the-art communication circuit used, an optimized implementation with the use of an accurate RTC, and to the smart automatic management of the application by the WDC.

In addition to power consumption, time synchronization is also important, as it allows the current analysis system to correlate the measurements from different sensor nodes. The measurement timestamp is defined as the instant at which the current sensor is turned on. To measure it, the SN captures its local time at the beginning of the reception of every beacon (reception start interrupt). When the sensor is turned on, the SN computes the time difference between that instant and the reception time of the latest beacon. This time difference is transmitted to the WDC with the measurement data and the beacon sequence number related to the time capture. Upon receiving a measurement packet, the WDC computes the timestamp starting from the beacon transmission time, looked up in a table using the beacon sequence number received in the data packet. Finally, the timestamp is computed by adding the time difference, as read from the data packet, to the beacon transmission time.

Synchronization accuracy was measured with a logic analyzer connected to debug pins of the communication board of both the WDC and the SN as the difference between the beacon-measurement delay reported by the SN to the WDC and the same delay as observed on the logic analyzer. Tests performed on 10 different SN devices show an error of 9  $\mu\text{s}$  - 12  $\mu\text{s}$  between SN and WDC time.

## V. THE WSN SYSTEM AS A WHOLE

Flight qualification tests of the complete WSN were performed at an industrial avionics qualifications facility. The evaluation setup with two sensor nodes under test on the full-scale aircraft beam testbed are shown in Fig. 18 and Fig. 19. Wireless communications including multi sensor node pairing and scheduled measurement packet delivery were demonstrated,

using two inductive energy harvesting powered sensor nodes. A measured power consumption profile of the communication PCB during a cycle of beacon reception, data acquisition and data transmission is shown in Fig. 20. The cycle duration and average current consumption are 5 ms and 6.84 mA respectively, demonstrating successful network operation of the SN. As a network level functionality example, indicative current monitoring data, as received by the WDC during application of different uncalibrated current values on the aircraft structural beam at 360 Hz are shown in Fig. 21.

The total power requirements of each sensor node during network association and data acquisition were measured to be 1.1 mW and 0.96 mW respectively. These measurements agree well with the 1.1 mW power consumption observed in the harvesting power supply tests of Fig. 13.

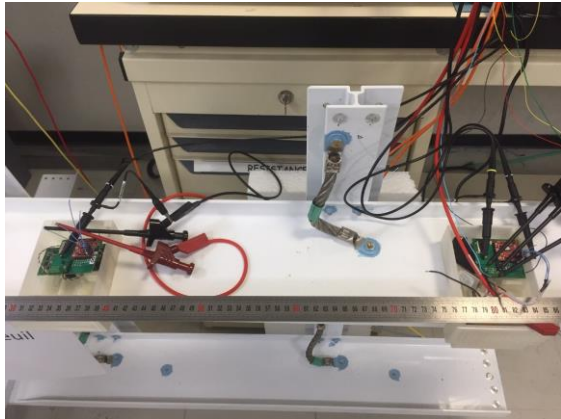


Fig. 18: Two sensor nodes installed on the aircraft structural beam testbed, under test while paired to the Wireless Data Concentrator (WDC).

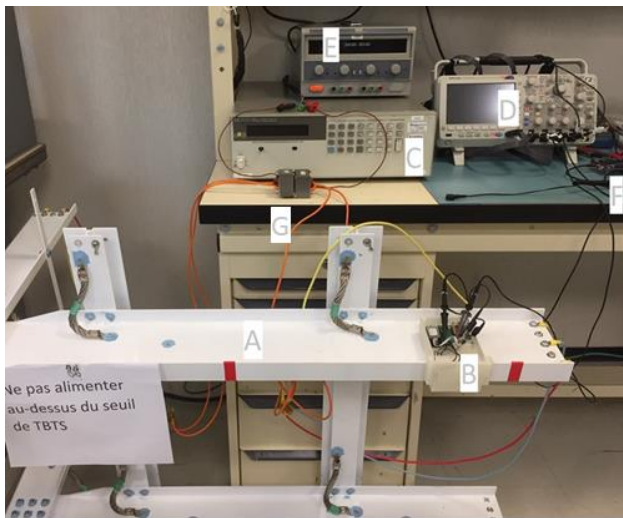


Fig. 19: Overview of the test bed showing the testbed instrumentation including two sensor node locations (A and B), the structural current signal generator (C), a monitoring oscilloscope (D), a DC power supply (E), an inductive current probe (F, partially shown) and a current transformer (G). At the time the photo was taken, the sensor node at location A was being tested elsewhere.



Fig. 20: Communication PCB power consumption during a beacon reception, acquisition and data transmission cycle. The sensor PCB current consumption is not included in this measurement.

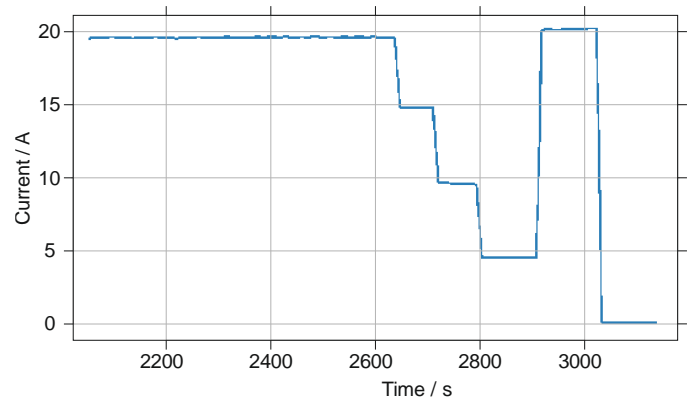


Fig. 21: Indicative, uncalibrated AC current monitoring data from a SN as collected by a WDC, while a series of different AC current values were being applied on the aircraft structural beam for testing.

## VI. CONCLUSION

An energy autonomous WSN for monitoring the structural return current path on aircraft during flight was demonstrated. This was enabled by the introduction of a hybrid inductive and hall effect differential sensor for structural currents in combination with hardware filtering for a flat frequency response, and a sensing power consumption of 35 mW. In addition, a low-power sensor node platform based on the Nordic Semiconductor nRF52840 system on chip was developed and programmed with a custom network operation protocol that enables duty cycling during both network association and acquisition/transmission. The implementation of this approach led to an average power requirement as low as 70  $\mu$ W for network association and 50  $\mu$ W for acquisition/transmission, comparable to the 37  $\mu$ W of sleep mode consumption. At this power level, power autonomy is limited by sleep mode consumption and capacitor leakage.

An inductive energy harvesting approach based on magnetic flux funnelling was adopted and a cold-starting bipolar power management circuit with reactance cancellation, maximum power point tracking and supercapacitor storage was introduced. The harvesting system was demonstrated to provide 0.13 mW of net power to the sensor node system, from a 20 A RMS, 360 Hz structural distributed current (65  $\mu$ T RMS field).

The overall power requirement of the sensor node system including leakage was measured to be around 1 mW. This allowed the demonstration of sensor node functionality for around 1 minute every 8 minutes of energy harvesting. Given that the measurement acquisition and transmission duration is in the 10 ms range and that the power consumption is sleep-mode dominated, this functionality rate allows a measurement rate of at least one sample every 8 minutes as required by the use case specifications. Higher or lower rates may be expected from higher or lower structural current values. Power autonomy duration can be adjusted by supercapacitor storage selection.

A summary of the WSN monitoring system features is presented in Table IV, in comparison with the use case target specifications. The RF communication platform, in combination with the central time-stamping functionality supported by the TDMA protocol allows independent synchronized functionality of multiple wireless sensor concentrators (WDC) and sensor nodes per WDC, for over 300 sensor nodes. It is noted that in multiple sensor node deployment, each sensor node includes its own inductive energy harvesting power supply module. Additional power consumption may occur only due to communication beacon conflicts or delays, which are expected to be minor due to the integrated multi-channel support and to the time-slot association protocol architecture. The successful demonstration of power autonomous operation of the introduced structural current monitoring system offers a WSN platform for the development of other, multi-sensor autonomous systems for aircraft.

TABLE IV  
DEMONSTRATED WSN PERFORMANCE VS USE CASE SPECIFICATIONS

Use Case Specification	Demonstrated Performance
Measurement range 5 A -100 A, DC-800 Hz	5 A -100 A, DC-800 Hz
Measurement resolution 0.5 A	< 0.5 A
Measurement accuracy 1%	< 2%
Up to 300 nodes, 30 m range	Supported by RF platform
One measurement / 8 minutes	One measurement / 8 min
Power Autonomy	1 min every 8 mins at 20 A
Measurement synchronization 1 ms	12 $\mu$ s

## REFERENCES

- [1] B. Systems. (2022, 17.01.2022). *Aircraft Electrification*. Available: <https://www.baesystems.com/en-us/product/aircraft-electrification>
- [2] (2017). *Aviation Depends On Sensors And Big Data*. Available: [https://siliconsemiconductor.net/article/102842/Aviation\\_depends\\_on\\_sensors\\_and\\_big\\_data](https://siliconsemiconductor.net/article/102842/Aviation_depends_on_sensors_and_big_data)
- [3] M. Heinen, "The A380 program," in *Global Investor Forum*, 2006: EADS.
- [4] H. L. Fu, Z. Sharif-Khodaei, and M. H. F. Aliabadi, "An energy-efficient cyber-physical system for wireless on-board aircraft structural health monitoring," *Mechanical Systems and Signal Processing*, vol. 128, pp. 352-368, Aug 2019.
- [5] H. Fu, Z. S. Khodaei, and M. H. F. Aliabadi, "An Event-Triggered Energy-Efficient Wireless Structural Health Monitoring System for Impact Detection in Composite Airframes," *IEEE Internet of Things Journal*, vol. 6, no. 1, pp. 1183-1192, 2019.
- [6] Y. Wang, L. Qiu, Y. J. Luo, R. Ding, and F. Jiang, "A piezoelectric sensor network with shared signal transmission wires for structural health monitoring of aircraft smart skin," *Mechanical Systems and Signal Processing*, vol. 141, Jul 2020, Art. no. 106730.
- [7] L. v. Allmen *et al.*, "Aircraft Strain WSN powered by Heat Storage Harvesting," *IEEE Transactions on Industrial Electronics*, vol. 64, no. 9, pp. 7284-7292, 2017.
- [8] H. Kwon, Y. Park, C. Shin, J. H. Kim, and C. G. Kim, "In-Flight Strain Monitoring of Aircraft Tail Boom Structure Using a Fiber Bragg Grating Sensor Based Health and Usage Monitoring System," *International Journal of Aeronautical and Space Sciences*, vol. 22, no. 3, pp. 567-577, Jun 2021.
- [9] J. Pytka, J. Jozwik, T. Lyszczczyk, E. Gnapowski, and Ieee, "Embedded Wheel Force Sensor For Aircraft Landing Gear Testing," in *5th IEEE International Workshop on Metrology for AeroSpace (MetroAeroSpace)*, Rome, Italy, 2018, pp. 74-78, 2018.
- [10] G. Yan, T. Q. Wang, L. Q. Zhu, F. Y. Meng, and W. Zhuang, "A novel strain-decoupled sensitized FBG temperature sensor and its applications to aircraft thermal management," *Optics and Laser Technology*, vol. 140, Aug 2021, Art. no. 106597.
- [11] J. P. Leitzke, A. Della Mea, L. M. Faller, S. Muhlbacher-Karrer, and H. Zangl, "Wireless differential pressure measurement for aircraft," *Measurement*, vol. 122, pp. 459-465, Jul 2018.
- [12] R. Samano *et al.*, "Active flow control using dense wireless sensor and actuator networks," *Microprocessors and Microsystems*, vol. 61, pp. 279-295, Sep 2018.
- [13] S. Gao, F. Shang, and C. C. Du, "Design of Multichannel and Multihop Low-Power Wide-Area Network for Aircraft Vibration Monitoring," *IEEE Transactions on Instrumentation and Measurement*, vol. 68, no. 12, pp. 4887-4895, Dec 2019.
- [14] X. Wang, "Application of Portable Ultrasonic Flow Sensor in Aircraft Hydraulic System," in *2019 4th International Conference on Mechanical, Control and Computer Engineering (ICMCCE)*, 2019, pp. 247-2473.
- [15] M. Rhudy, "A Dynamic Model-Aided Sensor Fusion Approach to Aircraft Attitude Estimation," in *60th IEEE International Midwest Symposium on Circuits and Systems (MWSCAS)*, Tufts Univ, Medford Somerville Campus, Boston, MA, 2017, pp. 1406-1409, 2017.
- [16] C. H. Wu, J. G. Yan, H. Lin, X. W. Wu, and B. Xiao, "Fixed-time disturbance observer-based chattering-free sliding mode attitude tracking control of aircraft with sensor noises," *Aerospace Science and Technology*, vol. 111, Apr 2021, Art. no. 106565.
- [17] C. Tong *et al.*, "An innovative deep architecture for aircraft hard landing prediction based on time-series sensor data," *Applied Soft Computing*, vol. 73, pp. 344-349, Dec 2018.
- [18] H. Salehi, S. Das, S. Chakrabarty, S. Biswas, and R. Burgueno, "Damage identification in aircraft structures with self-powered sensing technology: A machine learning approach," *Structural Control & Health Monitoring*, vol. 25, no. 12, Dec 2018, Art. no. e2262.
- [19] S. H. Kim, J. W. Kim, D. S. Kim, and Ieee, "Performance analysis of Cooperative Schemes for Wireless Sensor Network of Aircraft," in *11th International Conference on Ubiquitous and Future Networks (ICUFN)*, Zagreb, CROATIA, 2019, pp. 642-645, 2019.
- [20] T. V. Fepeussi, Y. W. Jin, Y. Xu, D. Xiang, and F. Huo, "Acoustic Data Communication by Wireless Sensor Network on Plate-like Structures for Autonomous Structural Health Monitoring of Aerovehicles," in *Conference on Autonomous Systems - Sensors, Vehicles, Security, and the Internet of Everything*, Orlando, FL, 2018, vol. 10643, pp. 114-127, 2018.
- [21] F. Y. Wan, X. L. Yu, Q. Yu, and Ieee, "Research on Optimal Sensor Placement for Aircraft Structural Health Management," in *IEEE International Conference on Prognostics and Health Management (ICPHM)*, Dallas, TX, 2017, pp. 160-166, 2017.
- [22] A. Aglargo, A. Bierig, A. Reinhardt, and Ieee, "Dynamic Reconfigurability of Wireless Sensor and Actuator Networks in Aircraft," in *IEEE International Conference on Wireless for Space and Extreme Environments (WiSEE)*, Montreal, CANADA, 2017, pp. 1-6, 2017.
- [23] D. Krichen, W. Abdallah, and N. Boudriga, "On the design of an embedded wireless sensor network for aircraft vibration monitoring using efficient game theoretic based MAC protocol," *Ad Hoc Networks*, vol. 61, pp. 1-15, Jun 2017.
- [24] J. K. Zhang *et al.*, "Aeronautical Ad Hoc Networking for the Internet-Above-the-Clouds," *Proceedings of the IEEE*, vol. 107, no. 5, pp. 868-911, May 2019.
- [25] P. Park, P. Di Marco, J. Nah, and C. Fischione, "Wireless Avionics Intracommunications: A Survey of Benefits, Challenges, and Solutions," *IEEE Internet of Things Journal*, vol. 8, no. 10, pp. 7745-7767, May 2021.
- [26] B. Zaghari *et al.*, "High-Temperature Self-Powered Sensing System for a Smart Bearing in an Aircraft Jet Engine," *IEEE Transactions on Instrumentation and Measurement*, vol. 69, no. 9, pp. 6165-6174, Sept 2020.
- [27] T. Becker, A. Elefsiniotis, and M. E. Kiziroglou, "Thermoelectric Energy Harvesting in Aircraft," in *Micro Energy Harvesting: Wiley-VCH Verlag GmbH & Co. KGaA*, 2015, pp. 415-434.

- [28] T. T. Toh, S. W. Wright, M. E. Kiziroglou, P. D. Mitcheson, and E. M. Yeatman, "A dual polarity, cold-starting interface circuit for heat storage energy harvesters," *Sensors and Actuators A: Physical*, vol. 211, no. 0, pp. 38-44, 2014.
- [29] M. E. Kiziroglou, S. W. Wright, T. T. Toh, P. D. Mitcheson, T. Becker, and E. M. Yeatman, "Design and Fabrication of Heat Storage Thermoelectric Harvesting Devices," *Industrial Electronics, IEEE Transactions on*, vol. 61, no. 1, pp. 302-309, 2014.
- [30] Z. J. Chew, T. W. Ruan, and M. L. Zhu, "Strain Energy Harvesting Powered Wireless Sensor System Using Adaptive and Energy-Aware Interface for Enhanced Performance," *IEEE Transactions on Industrial Informatics*, vol. 13, no. 6, pp. 3006-3016, Dec 2017.
- [31] H. Phan *et al.*, "Aerodynamic and aeroelastic flutters driven triboelectric nanogenerators for harvesting broadband airflow energy," *Nano Energy*, vol. 33, pp. 476-484, Mar 2017.
- [32] M. E. Kiziroglou, T. Becker, E. M. Yeatman, U. Schmid, J. W. Evans, and P. K. Wright, "Comparison of methods for static charge energy harvesting on aircraft," in *SPIE Microtechnologies*, Barcelona, Spain, 2017, vol. 10246, pp. 231-236.
- [33] T. T. Toh, S. W. Wright, M. E. Kiziroglou, E. M. Yeatman, and P. D. Mitcheson, "Harvesting energy from aircraft power lines," in *Proceedings of the 1st International Workshop on Energy Neutral Sensing Systems*, 2013, p. 13: ACM.
- [34] M. E. Kiziroglou, S. W. Wright, and E. M. Yeatman, "Coil and core design for inductive energy receivers," *Sensors and Actuators A: Physical*, vol. 313, p. 112206, 2020/10/01/ 2020.
- [35] S. W. Wright, M. E. Kiziroglou, S. Spasic, N. Radosevic, and E. M. Yeatman, "Inductive Energy Harvesting From Current-Carrying Structures," *IEEE Sensors Letters*, vol. 3, no. 6, pp. 1-4, 2019.
- [36] M. E. Kiziroglou, S. W. Wright, and E. M. Yeatman, "Power Supply Based on Inductive Harvesting From Structural Currents," *IEEE Internet of Things Journal*, vol. 9, no. 10, pp. 7166-7177, 2022.
- [37] M. Tavana, M. Ozger, A. Baltaci, B. Schleicher, D. Schupke, and C. Cavdar, "Wireless Power Transfer for Aircraft IoT Applications: System Design and Measurements," *IEEE Internet of Things Journal*, vol. 8, no. 15, pp. 11834-11846, Aug 2021.
- [38] C. V. Pham, T. A. Vu, W. Tran, A. V. Pham, C. Gardner, and Ieee, "Wireless Energy Harvesting System Through Metal for Aerospace Sensor," in *IEEE Transportation and Electrification Conference and Expo (ITEC)*, Long Beach, CA, 2018, pp. 545-549, 2018.
- [39] P. Sundriyal and S. Bhattacharya, "Energy Harvesting Techniques for Powering Wireless Sensor Networks in Aircraft Applications: A Review," 2019, pp. 55-76.
- [40] S. Zelenika *et al.*, "Energy Harvesting Technologies for Structural Health Monitoring of Airplane Components—A Review," *Sensors*, vol. 20, no. 22, p. 6685, 2020.
- [41] T. Toh *et al.*, "Inductive energy harvesting from variable frequency and amplitude aircraft power lines," *Journal of Physics: Conference Series*, vol. 557, no. 1, p. 012095, 2014.
- [42] H. H. Sample, W. J. Bruno, S. B. Sample, and E. K. Sichel, "Reverse-field reciprocity for conducting specimens in magnetic fields," *Journal of Applied Physics*, vol. 61, no. 3, pp. 1079-1084, 1987.
- [43] (2021, 04/09/2021). *Holland Shielding Systems B.V. Magnetic Shielding, Mu ferro-HD 6800 Series Technical Datasheet*. Available: <https://hollandshielding.com/Mu-ferro-HD>
- [44] S. W. Wright, M. E. Kiziroglou, and E. M. Yeatman, "Magnetic Flux Guidance Using H Structures for Miniature Transducers," presented at the PowerMEMS 2021, 2021.
- [45] Comchip. (2022, 11.02.2022). *Comchip SMD Schottky Barrier Diodes, RB521G-30HF*. Available: <https://www.comchiptech.com/product.php?id=3567>
- [46] "Texas Instruments BQ25570 nano power boost charger and buck converter for energy harvester powered applications," 2019, Available: [www.ti.com/product/BQ25570](http://www.ti.com/product/BQ25570).
- [47] A. S. Holmes and S. K. E. Yang, "Robust and Highly Efficient Active Rectifier for Low-Voltage Energy Harvesters," *To be published*, 2021.
- [48] (2019). *Maxim Integrated, MAX17220-MAX17225 400mV to 5.5V Input, nanoPower Synchronous Boost Converter with True Shutdown, 19-8753, Rev 4*. Available: <https://www.maximintegrated.com/en/products/power/switching-regulators/MAX17222.html>
- [49] K. Langendoen and A. Meier, "Analyzing MAC protocols for low data-rate applications," *ACM Trans. Sen. Netw.*, vol. 7, no. 2, p. Article 19, 2010.
- [50] M. Zohaib and T. M. Jadoon, "Comparison of S-MAC & TDMA-W Protocols for Energy Efficient Wireless Sensor Networks," in *2006 International Conference on Emerging Technologies*, 2006, pp. 486-492.
- [51] G. Mihai, D. A. Alina, and B. Ion, "Performance analysis on T-MAC protocol over a body area network," in *2010 3rd International Symposium on Electrical and Electronics Engineering (ISEEE)*, 2010, pp. 224-227.
- [52] A. Kumar, M. Zhao, K. J. Wong, Y. L. Guan, and P. H. J. Chong, "A Comprehensive Study of IoT and WSN MAC Protocols: Research Issues, Challenges and Opportunities," *IEEE Access*, vol. 6, pp. 76228-76262, 2018.
- [53] R. Tjoa, K. L. Chee, P. K. Sivaprasad, S. V. Rao, and J. G. Lim, "Clock drift reduction for relative time slot TDMA-based sensor networks," in *2004 IEEE 15th International Symposium on Personal, Indoor and Mobile Radio Communications (IEEE Cat. No.04TH8754)*, 2004, vol. 2, pp. 1042-1047 Vol.2.
- [54] S. Gobriel, D. Mosse, and R. Cleric, "TDMA-ASAP: Sensor Network TDMA Scheduling with Adaptive Slot-Stealing and Parallelism," in *2009 29th IEEE International Conference on Distributed Computing Systems*, 2009, pp. 458-465.
- [55] Y. Chen, Q. Zhao, V. Krishnamurthy, and D. Djonin, "Transmission Scheduling for Optimizing Sensor Network Lifetime: A Stochastic Shortest Path Approach," *IEEE Transactions on Signal Processing*, vol. 55, no. 5, pp. 2294-2309, 2007.
- [56] G. P. Halkes and K. G. Langendoen, "Crankshaft: An Energy-Efficient MAC-Protocol for Dense Wireless Sensor Networks," in *Wireless Sensor Networks*, Berlin, Heidelberg, 2007, pp. 228-244: Springer Berlin Heidelberg.
- [57] A. El-Hoiydi, J.-D. Decotignie, C. Enz, and E. Leroux, *WiseMAC, an ultra low power MAC protocol for the wiseNET wireless sensor network*. 2003, pp. 302-303.